

A priori mesh quality metric error analysis applied to a high-order finite element method

W. Lowrie^{a,*}, V.S. Lukin^b, U. Shumlak^a

^a Plasma Science and Innovation Center, University of Washington, Box 352250 Seattle, WA 98195, United States

^b Space Science Division, Naval Research Laboratory, Code 7675L, 4555 overlook Ave Sw Washington, DC 20375, United States

ARTICLE INFO

Article history:

Received 1 September 2010

Received in revised form 15 February 2011

Accepted 18 March 2011

Available online 3 April 2011

Keywords:

Finite element

Spectral element

Mesh deformation

Mesh quality metrics

MHD

ABSTRACT

Characterization of computational mesh's quality prior to performing a numerical simulation is an important step in insuring that the result is valid. A highly distorted mesh can result in significant errors. It is therefore desirable to predict solution accuracy on a given mesh. The HiFi/SEL high-order finite element code is used to study the effects of various mesh distortions on solution quality of known analytic problems for spatial discretizations with different order of finite elements. The measured global error norms are compared to several mesh quality metrics by independently varying both the degree of the distortions and the order of the finite elements. It is found that the spatial spectral convergence rates are preserved for all considered distortion types, while the total error increases with the degree of distortion. For each distortion type, correlations between the measured solution error and the different mesh metrics are quantified, identifying the most appropriate overall mesh metric. The results show promise for future *a priori* computational mesh quality determination and improvement.

© 2011 Elsevier Inc. All rights reserved.

1. Introduction

Mesh quality metrics have been used widely to quantify the amount and character of distortion of computational meshes [1,2]. Many metrics do not show a strong global correlation to solution accuracy, mainly because of the variety of problems that have to be considered and complexity of correlating them to solution error [1–3,5]. Nevertheless, they can be used to find approximate relationships between mesh quality and solution error or to identify regions of a mesh that need repair. Here, several different mesh quality metrics are explored with the goal of finding a “universal metric” that can serve as a guide in predicting solution error magnitudes for different systems of equations. If achieved, this capability would enable a quantifiable measure of whether or not a mesh is of acceptable quality for a particular set of equations.

Little work has been performed on quantifying mesh quality for use in high-order finite element simulations. Most of the research to date has either been with finite volume methods [6–8] or linear finite element methods [1–3,9,5], though more recently quadratic finite elements have also been investigated [4]. In the finite volume case, a truncation error estimate based on the finite volume spatial discretization is commonly used. For the finite element method, the stiffness matrix condition number has been analyzed [10–12], where the stiffness matrix is formed by considering gradients of the linear finite element basis functions. This method naturally extends to high-order finite elements. More recent work [13] has examined a nodal spectral stiffness matrix for finite elements. In the research presented here, the spectral element stiffness matrix is calculated and used as one of the mesh quality metrics.

* Corresponding author. Tel.: +1 206 792 9037.

E-mail address: wlowrie@uw.edu (W. Lowrie).

The approach chosen in this work is to study elemental grid deformations that impact the shape of a single high order finite element or the interaction between two neighboring high order finite elements. In doing so, the effects of such deformations on the differential operators are isolated. Deformations are chosen that are commonly encountered when numerically solving partial differential equations (PDEs). In the following sections, the global effects of the individual mesh distortions on solution quality are explored for known analytic problems by independently varying both the degree of the distortions and the order of the finite elements. Several previously published mesh quality metrics are compared to the measured global solution error generated from high order finite element spatial discretizations.

A brief overview of the high-order finite element method is described in Section 2 and the logical-to-physical coordinate transformation is formulated in the HiFi/SEL code to show the effect of coordinate transformation on the resulting system of equations. Section 3 outlines several distortion classifications: stretch, shear and skew. For each distortion type, a Jacobian is calculated to understand when a particular deformation type becomes degenerate. Candidate mesh quality metrics are described in Section 4. These metrics are used to analyze each of the different distortion types. A representative mesh is analyzed with the different metrics and then compared to solutions of three equation sets (linear advection, Poisson’s equation, and linearized MHD). These test problems have known analytic solutions. Section 5 outlines the three test problems, and Section 6 presents the analysis of the mesh metrics and the test problem solutions.

2. High-order finite element method

In the following analysis, the HiFi/SEL [14–16] high-order finite element code is used. The code uses a flux-source formulation, which makes specifying any particular set of partial differential equations straightforward. This enables analysis of various PDE systems while using the same formulation and meshes.

2.1. Flux-source equation form

The flux-source equation form is a simple way of representing many equations:

$$\frac{\partial \vec{Q}}{\partial t} + \nabla \cdot \vec{F} = \vec{S}, \tag{2.1}$$

where \vec{Q} is a vector of dependent variables, and \vec{F} and \vec{S} are vectors of fluxes and sources associated with each of the variables. Any equation that can be represented in this form can be implemented into the HiFi/SEL framework. HiFi is three-dimensional (3D) and SEL is two-dimensional (2D); their formulation is identical and discussion is limited here to the 2D SEL code.

2.2. Logical to physical grid transformation

The SEL solver uses a logical square of quadrilateral elements with coordinates:

$$(\xi, \eta) \in \Omega_e : [0, 1] \times [0, 1]. \tag{2.2}$$

The logical dimensions are transformed to some physical coordinates x and y of arbitrary range, such that $x = x(\xi, \eta)$ and $y = y(\xi, \eta)$.

To demonstrate how the transformation fits into the solver consider Poisson’s equation:

$$\nabla^2 \phi(x, y) = S(x, y), \tag{2.3}$$

where $\phi(x, y)$ is some scalar variable and $S(x, y)$ is some source forcing function. For this equation to fit into the flux-source form, it is rewritten as:

$$\frac{\partial \phi}{\partial t} + \nabla \cdot \vec{F}(x, y) = S(x, y), \tag{2.4}$$

where $\vec{F}(x, y) = \nabla \phi(x, y)$. The equation is rewritten in terms of the logical coordinates ξ and η , and multiplied by the Jacobian J . This multiplication by the Jacobian is important, because J can potentially become singular for certain grid distortions. In logical metric space, the equation is written as:

$$\frac{\partial}{\partial \xi} \left[(\nabla \phi \cdot \nabla x) J \frac{\partial \xi}{\partial x} + (\nabla \phi \cdot \nabla y) J \frac{\partial \xi}{\partial y} \right] + \frac{\partial}{\partial \eta} \left[(\nabla \phi \cdot \nabla x) J \frac{\partial \eta}{\partial x} + (\nabla \phi \cdot \nabla y) J \frac{\partial \eta}{\partial y} \right] JS, \tag{2.5}$$

where

$$J = \begin{vmatrix} \frac{\partial x}{\partial \xi} & \frac{\partial x}{\partial \eta} \\ \frac{\partial y}{\partial \xi} & \frac{\partial y}{\partial \eta} \end{vmatrix} = \frac{\partial x}{\partial \xi} \frac{\partial y}{\partial \eta} - \frac{\partial x}{\partial \eta} \frac{\partial y}{\partial \xi}. \tag{2.6}$$

2.3. Weak form of equations

In the SEL solver, PDEs are transformed into the weak form by projecting the solution onto a polynomial basis. With the Galerkin discretization, Eq. (2.5) in weak form becomes:

$$\int_{\Omega_e} \left[F_x \left(\frac{\partial \xi}{\partial x} \frac{\partial \alpha^i}{\partial \xi} + \frac{\partial \eta}{\partial x} \frac{\partial \alpha^i}{\partial \eta} \right) + F_y \left(\frac{\partial \xi}{\partial y} \frac{\partial \alpha^i}{\partial \xi} + \frac{\partial \eta}{\partial y} \frac{\partial \alpha^i}{\partial \eta} \right) - S \alpha^i \right] J d\xi d\eta = 0, \tag{2.7}$$

where $\alpha^i(\xi, \eta)$ is a 2D basis (trial) function polynomial defined in the domain Ω_e , and

$$F_x = \frac{\partial \phi}{\partial x} \quad \text{and} \quad F_y = \frac{\partial \phi}{\partial y}. \tag{2.8}$$

The weak form equation is solved for every element in the domain. Notice the fluxes F_x and F_y are multiplied by grid metrics of the logical coordinates with respect to the physical coordinates, and the whole equation is integrated in the logical metric space.

The derivatives of the basis functions ($\frac{\partial \alpha^i}{\partial \xi}$ and $\frac{\partial \alpha^i}{\partial \eta}$) are known exactly, since the chosen basis functions have analytical derivatives. The grid metrics $\frac{\partial \xi}{\partial x}$, $\frac{\partial \xi}{\partial y}$, $\frac{\partial \eta}{\partial x}$, and $\frac{\partial \eta}{\partial y}$ must also be known in order to integrate the equation and solve for $\phi(x, y)$. These grid metrics can be represented in terms of the Jacobian and derivatives of the physical coordinates with respect to the logical coordinates:

$$\begin{aligned} \frac{\partial \xi}{\partial x} &= \frac{1}{J} \frac{\partial y}{\partial \eta}, & \frac{\partial \xi}{\partial y} &= -\frac{1}{J} \frac{\partial x}{\partial \eta}, \\ \frac{\partial \eta}{\partial x} &= -\frac{1}{J} \frac{\partial y}{\partial \xi}, & \frac{\partial \eta}{\partial y} &= \frac{1}{J} \frac{\partial x}{\partial \xi}, \end{aligned} \tag{2.9}$$

where the Jacobian J is given by Eq. (2.6).

3. Grid distortions from a logical square

The logical to physical transformation introduces distortions, and often in order to achieve the desired physical shapes, the distortions can be severe. Mapping the logical square to a physical circle is an extreme example of this, where “the corners” of the circle have large and singular angle distortions. Fig. 1 shows an example square mesh distorted into a circular shape. Here, in order to capture most of the basic distortion types, the distortions are classified into *stretch*, *shear*, *skew*, *large angle*, and *small edge*. This is not intended to be a complete set of distortions but provides a set of typical elemental grid deformations that are commonly encountered in real meshes. The goal of this study is to evaluate solution error due to such elemental distortions of single high order elements (e.g. shear) and interactions between two neighboring differently distorted high order elements (e.g. skew).

Definitions of these different distortions, the logical to physical mapping, and the grid Jacobians for each type are shown in the following sections.

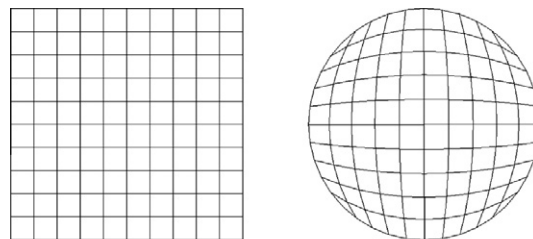
3.1. Stretch

Stretching is the simplest mapping with

$$x(\xi, \eta) = l_x \xi, \tag{3.1}$$

$$y(\xi, \eta) = l_y \eta, \tag{3.2}$$

where l_x and l_y are the respective stretching factors for the x and y dimensions (see Fig. 2). The values of l_x and l_y do not have to be equal, and situations could arise where $l_x \gg l_y$. The resulting Jacobian is:



(a) Square Mesh

(b) Circular Mesh

Fig. 1. An example 10 × 10 square mesh (a) and a circular mesh (b), where the circular mesh has a square to circle mesh transformation.

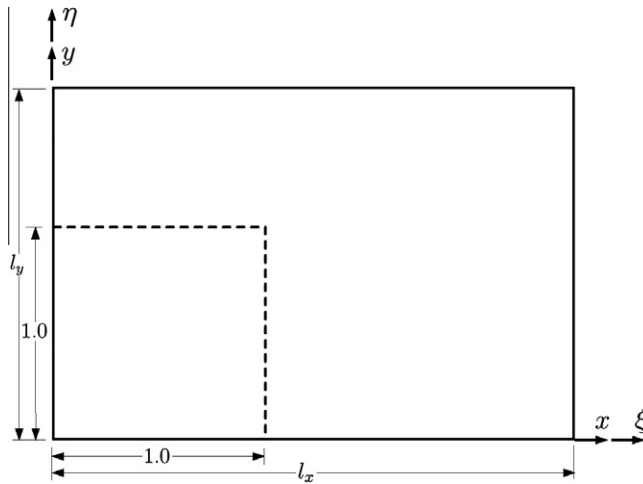


Fig. 2. A single element with stretch deformation magnitudes of l_x and l_y . The dashed line represents the undeformed logical element, and the solid line represents the deformed element.

$$J = \frac{\partial x}{\partial \xi} \frac{\partial y}{\partial \eta} - \frac{\partial x}{\partial \eta} \frac{\partial y}{\partial \xi} = l_x l_y. \tag{3.3}$$

It can be seen that the grid becomes degenerate when either l_x or l_y approach 0.

3.2. Shear

The shear mapping can be defined as:

$$x(\xi, \eta) = \xi + \eta \sin \theta, \tag{3.4}$$

$$y(\xi, \eta) = \eta \cos \theta, \tag{3.5}$$

where θ is the shear angle for the element (see Fig. 3). The Jacobian is:

$$J = \frac{\partial x}{\partial \xi} \frac{\partial y}{\partial \eta} - \frac{\partial x}{\partial \eta} \frac{\partial y}{\partial \xi} = \cos \theta. \tag{3.6}$$

In this case when $\theta \rightarrow \pi/2$, $J \rightarrow 0$ and the grid is considered degenerate. When the shear angle approaches $\pi/2$, the quadrilateral element has both small angles as well as obtuse angles, which can be problematic.

3.3. Skew

Skew involves an interaction between elements and cannot be classified in the same way as the stretch, and shear transformations. The skew can be seen as two adjacent elements with an angle ω between them (see Fig. 4). In the case shown in Fig. 4, the skewed mesh has a rectangular element adjacent to an element with a shear deformation. Each element has a separate Jacobian defined. The rectangular element has no deformation and the Jacobian is $J = 1$. The adjacent element is a sheared element with a transformation:

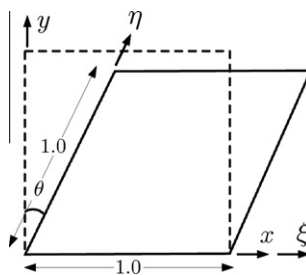


Fig. 3. A single element with a shear angle of θ . The dashed line represents the undeformed logical element, and the solid line represents the deformed element.

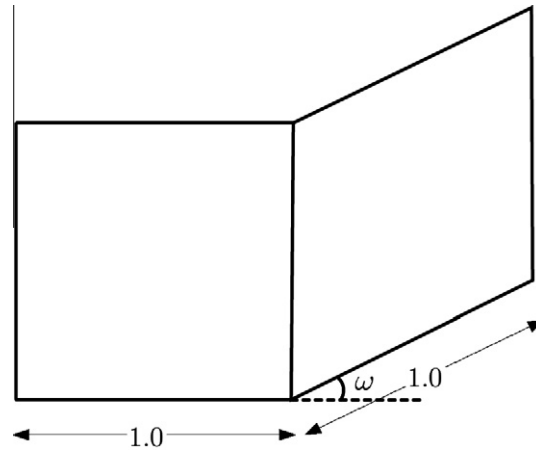


Fig. 4. Adjacent elements with a skew angle ω .

$$x(\xi, \eta) = \xi \cos \omega, \quad (3.7)$$

$$y(\xi, \eta) = \eta + \xi \sin \omega, \quad (3.8)$$

and the Jacobian is:

$$J = \frac{\partial x}{\partial \xi} \frac{\partial y}{\partial \eta} - \frac{\partial x}{\partial \eta} \frac{\partial y}{\partial \xi} = \cos \omega. \quad (3.9)$$

The important distinguishing feature of the skew case is that an undeformed element is adjacent a sheared element, and there is some skew interaction between the two elements.

3.4. Large angle

The large angle deformation mapping can be defined as:

$$x(\xi, \eta) = \xi + m_x \eta + b_x, \quad (3.10)$$

$$y(\xi, \eta) = \eta + m_y \xi + b_y, \quad (3.11)$$

where

$$m_x = (1 - 2\xi) \frac{\phi}{2}, \quad (3.12)$$

$$m_y = -(1 - 2\eta) \frac{\phi}{2}, \quad (3.13)$$

$$b_x = -(1 - 2\xi) \frac{\phi}{4}, \quad (3.14)$$

$$b_y = (1 - 2\eta) \frac{\phi}{4}. \quad (3.15)$$

The deformation parameter ϕ is in the range $[0, 1]$, where 0 is no deformation, and 1 is deformed such that the angle θ in Fig. 5 is 180° . The Jacobian is:

$$J = \frac{\partial x}{\partial \xi} \frac{\partial y}{\partial \eta} - \frac{\partial x}{\partial \eta} \frac{\partial y}{\partial \xi} = 1 + \phi(\xi - \eta). \quad (3.16)$$

In this case when $\phi = 0$, $J = 1$, which is the undeformed case. When $\phi = 1$ ($\theta = 180^\circ$), then $J = 1 + \xi - \eta$. This Jacobian does not necessarily imply that the element will be degenerate when the angle has opened up to 180° .

3.5. Small edge

The small edge deformation mapping is defined as:

$$x(\xi, \eta) = \xi, \quad (3.17)$$

$$y(\xi, \eta) = \eta + m_y \xi + b_y, \quad (3.18)$$

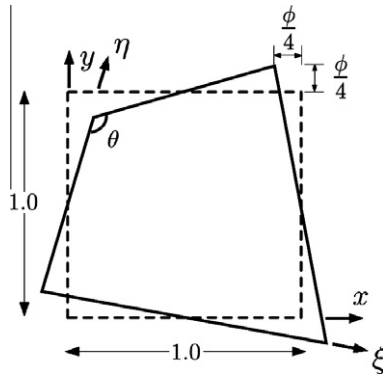


Fig. 5. A single element with a large angle deformation θ .

where

$$m_y = (1 - 2\eta)\phi, \tag{3.19}$$

$$b_y = -(1 - 2\eta) \frac{\phi}{2}. \tag{3.20}$$

The deformation parameter ϕ is in the range $[0, 1]$, where 0 is no deformation, and 1 is deformed such that one vertical edge has collapsed to a length of zero (Fig. 6). The opposite edge increases its length by the same amount the shrinking edge loses length. The Jacobian is defined as:

$$J = \frac{\partial x}{\partial \xi} \frac{\partial y}{\partial \eta} - \frac{\partial x}{\partial \eta} \frac{\partial y}{\partial \xi} = 1 - \phi(2\xi - 1), \tag{3.21}$$

and it can be seen that when $\phi = 1$, the Jacobian will be zero in the element, and thus it is degenerate.

4. Mesh quality metrics

In this study new mesh quality metrics are not defined, but instead previously published metrics are explored with the intent of correlating them to solution error in an *a priori* fashion. This does not mean that the metrics or the results of this study can only be used for *a priori* analysis, but that is the focus of the analysis presented here. (For instance, the same metrics could also be applied to *a posteriori* analysis of PDE solutions.)

A unique aspect of *a priori* analysis is that the mesh quality metrics depend solely on the mesh geometry and are independent of the equations being solved and of the solution itself. Here, the correlation between the solution error and the grid metrics is estimated by using equations that are representative of a physical problem. The fact that the metrics are independent of the representative equations makes correlation to solution error a challenge because there are no assumptions about

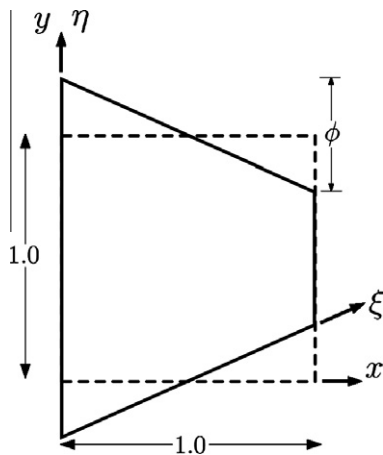


Fig. 6. A single element with a small edge deformation.

the physical problem at hand. At the same time, they can potentially be useful because the analysis can be applied before any numerical simulations are performed.

Three types of mesh quality metrics are explored. A set of metrics that deals with element to element interaction based on Kallinderis and Kontzialis [7] is the first type described in Section 4.1. A set of metrics based on an algebraic framework using the mesh Jacobian from Knupp [3] is explored in Section 4.2. The third type is based on the spectral element stiffness matrix condition number and described in Section 4.3.

4.1. Kallinderis/Kontzialis metrics

The mesh metric described in Kallinderis and Kontzialis [7] are based on analytic forms of the truncation error for the gradient operator. The error E is defined in terms of some variable u on the mesh:

$$E = \nabla^h u - \nabla^a u, \tag{4.1}$$

with the superscript h and a denoting the numerical and analytic gradients, respectively. The error is expanded in a Taylor series and can be grouped into different order terms. The coefficients for each order are used to calculate the metrics. For instance in 2D the first order terms are defined as:

$$e_{xy}^x = \frac{1}{2S} \sum_{e=1}^n (\Delta x_{e,1} \Delta y_{e,1} + \Delta x_{e,2} \Delta y_{e,2}) \Delta y_e, \tag{4.2}$$

$$e_{xx}^x = \frac{1}{2S2!} \sum_{e=1}^n ((\Delta x_{e,1})^2 + (\Delta x_{e,2})^2) \Delta y_e, \tag{4.3}$$

$$e_{yy}^x = \frac{1}{2S2!} \sum_{e=1}^n ((\Delta y_{e,1})^2 + (\Delta y_{e,2})^2) \Delta y_e, \tag{4.4}$$

where

$$(\Delta x_{e,k})^j (\Delta y_{e,k})^l = \frac{1}{N_{e,k}} \sum_{m=1}^{N_{e,k}} (x_{m|e,k} - x_0)^j (y_{m|e,k} - y_0)^l, \tag{4.5}$$

and $x_{m|e,k} - x_0, y_{m|e,k} - y_0$ are the coordinates offset from centroid, $N_{e,k}$ is total number of nodes associated with a dual vertex averaging, and S represents the area of the dual mesh. The subscript e represents the edge number and is defined on a dual mesh, which spans four elements in the structured quadrilateral mesh case. The spanning of four elements is the basis for the metric quantifying element to element interactions. Both first and second order metrics are defined (in 2D) and are normalized using a length scale of the elements. Eqs. (4.6) and (4.7) show the first order metrics, where the error coefficients defined in Eqs. (4.2), (4.3) and (4.4) are normalized by a characteristic length scale. The characteristic length scales for a uniform structured mesh are simply the element edge lengths. The normalized metrics are denoted with a over bar:

$$Q_x = |\bar{e}_{xx}^x| + |\bar{e}_{yy}^x| + |\bar{e}_{xy}^x|, \tag{4.6}$$

$$Q_y = |\bar{e}_{xx}^y| + |\bar{e}_{yy}^y| + |\bar{e}_{xy}^y|. \tag{4.7}$$

More details about the calculation of the metrics are in Kallinderis and Kontzialis [7].

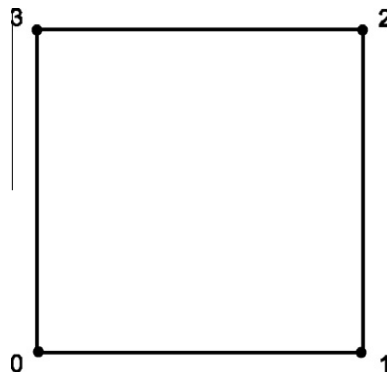


Fig. 7. An example Knupp reference quadrilateral.

4.2. Knupp metrics

Knupp’s metrics are defined by an algebraic framework described in [3], and in more detail in [1]. They are based upon the mesh Jacobian A_k for linear finite elements. The metric is a local (element wise) metric compared against some reference quadrilateral (see Fig. 7). The indexing k is counterclockwise around the element, and is modulo three, such that if $k = 2$, then $k + 1$ becomes 0, and $k + 2$ becomes 1 [3]. The Jacobian is defined as:

$$A_k = \begin{pmatrix} x_{k+1} - x_k & x_{k+3} - x_k \\ y_{k+1} - y_k & y_{k+3} - y_k \end{pmatrix}. \tag{4.8}$$

From this Jacobian A_k , four ‘metric’ tensor matrices are defined:

$$\lambda_{ij}^k = \left(A_k^T A_k \right)_{ij}, \tag{4.9}$$

where the superscript T denotes transpose, and the λ_{ij}^k denotes the ij th element of k th metric tensor. Additionally, the parameter α_k is defined as the determinant of the Jacobian matrix:

$$\alpha_k = \det(A_k), \tag{4.10}$$

and τ_k as:

$$\tau_k = (\alpha_k + \alpha_{k+2})/2w, \tag{4.11}$$

where w is the total area of a reference quadrilateral, and the undeformed element area is used as the reference quadrilateral in the subsequent analysis. From these four parameters one can define three different mesh quality metrics.

A size metric is defined as:

$$f_{size} = \min(\tau_k, 1/\tau_k), \tag{4.12}$$

which compares the element of interest’s area to the area w of a reference quadrilateral element. This metric has the property of being 1 if and only if the quadrilateral has the same total area as the reference quadrilateral, and the metric is 0 if and only if the quadrilateral has a total area of zero [3].

The second metric is a shape metric:

$$f_{shape} = \frac{8}{\sum_{k=0}^3 (\lambda_{11}^k + \lambda_{22}^k) / (\alpha_k)}, \tag{4.13}$$

which compares the shape of an element to a square reference element. It has the properties of being 1 if and only if the quadrilateral is a square, and 0 if the quadrilateral is degenerate. It also has the property of being scale invariant [3].

The third metric is called the skew metric and is defined as:

$$f_{skew} = \frac{4}{\sum_{k=0}^3 \left(\sqrt{\lambda_{11}^k + \lambda_{22}^k} \right) / (\alpha_k)}, \tag{4.14}$$

which detects distortions based on angles within the element. It has a rectangular reference element and has the properties of being 1 if and only if the quadrilateral is a rectangle, and 0 if and only if the quadrilateral is degenerate. The metric is also scale invariant and independent of element edge length ratios [3]. The name of the skew metric should not be confused with the skew deformation as defined in Section 3.3. The metric measures angles in an element which could arise from either a *shear* or *skew* deformation.

A unique feature of the Knupp metrics is their range from 1 (undeformed) to 0 (degenerate), which allows for a combined metric by forming their product. The range of 1–0 remains and only the metrics that detect deformation will contribute to the product. The products of the size and shape metrics, as well as the size and skew metrics, are useful because they do not require a choice of which metric to use for different types of distortions. In the subsequent analysis these products are used as metrics. The shape and skew metrics are not combined together because they both account for the skew deformation.

4.3. Spectral stiffness matrix

The stiffness matrix condition number has previously been used to estimate the quality of a mesh. Zgainski et al. [12], as well as Tsukerman [11] explore properties of the finite element stiffness matrix in order to estimate solution accuracy. Zgainski specifically looks at the stiffness matrix condition number, while Tsukerman looks at the eigenvalues of the stiffness matrix. As noted by Tsukerman, this is also related to the ‘‘maximum angle’’ condition studied by Babuška and Aziz [9].

Here, the spectral element stiffness matrix is used as a metric. The matrix is defined globally (for the whole domain) and the eigenvalues then correspond to the problem area in the mesh. The method for creating the stiffness matrix and calculating its condition number is described.

4.3.1. Matrix construction

The 2D gradient operator is defined in terms of the logical coordinates as:

$$\nabla = \begin{bmatrix} \frac{\partial}{\partial x} \\ \frac{\partial}{\partial y} \end{bmatrix} = \begin{bmatrix} \frac{\partial \xi}{\partial x} \frac{\partial}{\partial \xi} + \frac{\partial \eta}{\partial x} \frac{\partial}{\partial \eta} \\ \frac{\partial \xi}{\partial y} \frac{\partial}{\partial \xi} + \frac{\partial \eta}{\partial y} \frac{\partial}{\partial \eta} \end{bmatrix}. \quad (4.15)$$

Using the mesh metrics from Eq. 2.9, the gradient operator becomes:

$$\nabla = \begin{bmatrix} \frac{1}{J} \frac{\partial y}{\partial \eta} \frac{\partial}{\partial \xi} - \frac{1}{J} \frac{\partial y}{\partial \xi} \frac{\partial}{\partial \eta} \\ -\frac{1}{J} \frac{\partial x}{\partial \eta} \frac{\partial}{\partial \xi} + \frac{1}{J} \frac{\partial x}{\partial \xi} \frac{\partial}{\partial \eta} \end{bmatrix}. \quad (4.16)$$

With the definition of the gradient operator from Eq. 4.16, the elements of the 2D stiffness matrix K are:

$$K^{ij} = \int_{\Omega} \nabla \alpha^i(\xi, \eta) \cdot \nabla \alpha^j(\xi, \eta) dx dy = \int_{\Omega} \nabla \alpha^i(\xi, \eta) \cdot \nabla \alpha^j(\xi, \eta) J d\xi d\eta, \quad (4.17)$$

where α^i and α^j are the 2D basis functions, and the integrand can be expanded as:

$$\begin{aligned} \nabla \alpha^i(\xi, \eta) \cdot \nabla \alpha^j(\xi, \eta) &= \frac{\partial \xi}{\partial x} \frac{\partial \xi}{\partial x} \frac{\partial \alpha^i}{\partial \xi} \frac{\partial \alpha^j}{\partial \xi} + \frac{\partial \eta}{\partial x} \frac{\partial \eta}{\partial x} \frac{\partial \alpha^i}{\partial \eta} \frac{\partial \alpha^j}{\partial \eta} + \frac{\partial \xi}{\partial x} \frac{\partial \eta}{\partial x} \frac{\partial \alpha^i}{\partial \xi} \frac{\partial \alpha^j}{\partial \eta} + \frac{\partial \eta}{\partial x} \frac{\partial \xi}{\partial x} \frac{\partial \alpha^i}{\partial \eta} \frac{\partial \alpha^j}{\partial \xi} + \frac{\partial \xi}{\partial y} \frac{\partial \xi}{\partial y} \frac{\partial \alpha^i}{\partial \xi} \frac{\partial \alpha^j}{\partial \xi} + \frac{\partial \eta}{\partial y} \frac{\partial \eta}{\partial y} \frac{\partial \alpha^i}{\partial \eta} \frac{\partial \alpha^j}{\partial \eta} \\ &\quad \times \frac{\partial \alpha^i}{\partial \eta} \frac{\partial \alpha^j}{\partial \eta} + \frac{\partial \eta}{\partial y} \frac{\partial \xi}{\partial y} \frac{\partial \alpha^i}{\partial \eta} \frac{\partial \alpha^j}{\partial \xi} + \frac{\partial \xi}{\partial y} \frac{\partial \eta}{\partial y} \frac{\partial \alpha^i}{\partial \xi} \frac{\partial \alpha^j}{\partial \eta}. \end{aligned} \quad (4.18)$$

The integral is numerically approximated using Gaussian quadrature:

$$K^{ij} = \int_{\Omega} [\nabla \alpha^i(\xi, \eta) \cdot \nabla \alpha^j(\xi, \eta)] J d\xi d\eta = \sum_{k=1}^{nq} \sum_{l=1}^{nq} J_{kl} W_{kl} [\nabla \alpha^i(\xi_k, \eta_l) \cdot \nabla \alpha^j(\xi_k, \eta_l)], \quad (4.19)$$

where nq is the number of quadrature points along each dimension, and W_{kl} is an array of weights at the quadrature points.

The full stiffness matrix can be constructed within the HiFi/SEL framework since all the derivatives of the logical variables and derivatives of the basis functions are known in the code.

4.3.2. Condition number calculation

The condition number of a matrix is defined as the ratio of the magnitude of its largest eigenvalue to its smallest eigenvalue, $|e_{\max}|/|e_{\min}|$. In the case of the global stiffness matrix, there is a null eigenvalue and therefore the smallest nonzero eigenvalue is used. These eigenvalues are calculated in parallel using the scalable library for eigenvalue problem computations (SLEPc) [17] solver package.

The condition number generally increases with resolution and with increasing spectral polynomial order, and must be normalized. A simple normalization by the total number of degrees of freedom ($nx \times ny \times np^2$) is sufficient for meaningful results, where nx and ny are the number of elements in the x and y directions respectively and np is the polynomial order of the basis function.

5. Test problems

In order to correlate the mesh quality metrics with solution error, three test problems are chosen. The advection equation is chosen to quantify mesh distortions on the ∇ operator, and Poisson's equation is chosen for the ∇^2 operator. These operators are some of the most common differential operators to be encountered in PDEs in fluid and plasma physics, and are therefore chosen to give the best indication of whether the mesh quality metrics could possibly predict solution error for practical problems of interest. Linearized MHD is also chosen to quantify solution error due mesh distortions for a more complex system of equations. All three test problems have simple analytical solutions, and therefore error norms could easily be calculated and compared to the different mesh quality metrics.

5.1. Meshes for testing deformation

Several model meshes (Fig. 8) are chosen for capturing the effects of different mesh distortions. Each mesh is intended to capture the effects of one of the grid distortions types described in Section 3. The meshes are chosen such that the distortion is repeated over the whole domain in a tiled or tessellated pattern. This allows the solution error due to each particular distortion to be studied separately, while the solution is evenly impacted by the distortion. It also allows for an arbitrarily large mesh at any resolution without impacting the distortion shape, and thus the interesting solution can be isolated from any solution boundary effects.

In order to eliminate boundary effects for both the advection equation and the linearized MHD equations, a doubly periodic domain is chosen. Additionally, in the advection case, the density advected is near zero at the boundary using a Gaussian

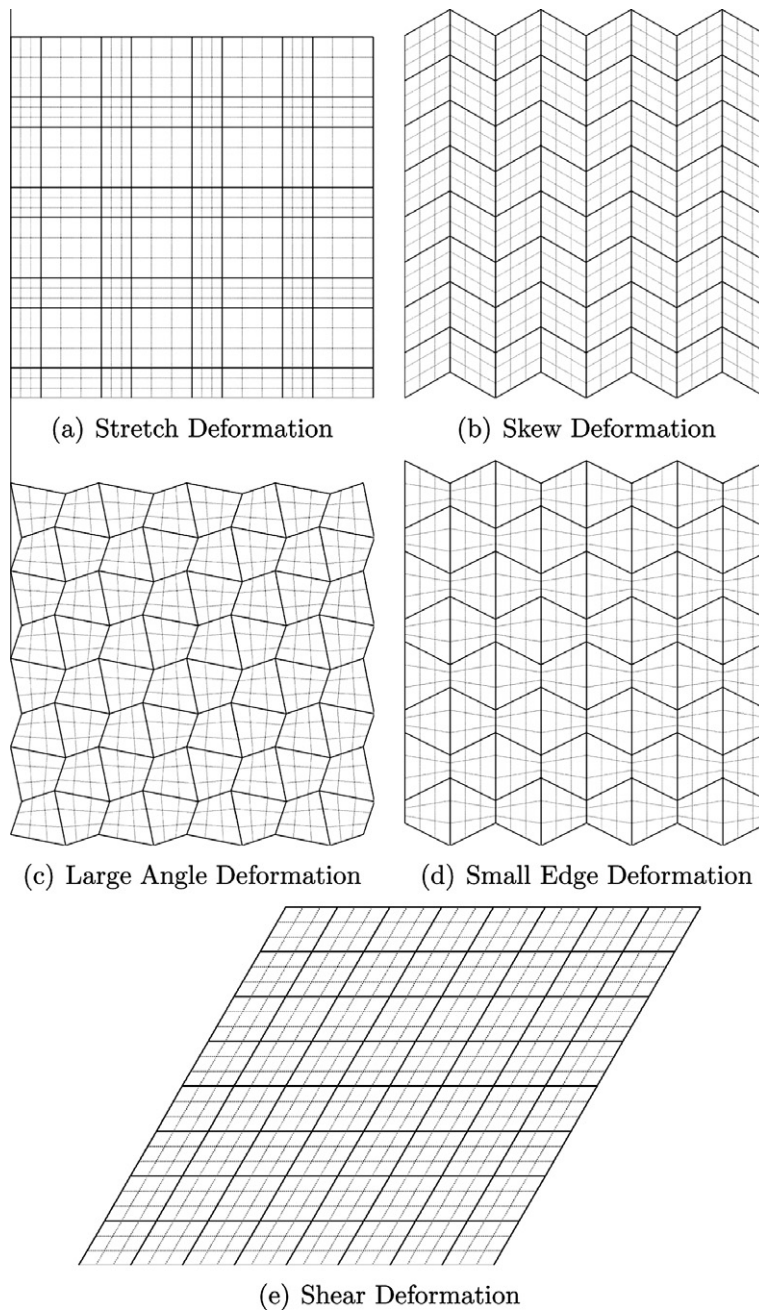


Fig. 8. Sample meshes for testing different distortion types. Grid resolution is $n_x = n_y = 8$ with $np = 3$. The solid lines represent the element boundaries and the dashed lines represent the interior distribution within the elements.

concentration in the domain centroid. Likewise, in the case of the Poisson equation, the source is centered in the domain and falls off to a near zero value at the boundary. Dirichlet boundary conditions are used to solve the Poisson equation.

5.2. Advection equation

A 2D advection equation is solved:

$$\frac{\partial \phi}{\partial t} + \nabla \cdot (\vec{c}\phi) = 0, \tag{5.1}$$

where ϕ is the Gaussian “density concentration” scalar, and $\vec{c} = [c_x, c_y]$ is the advection “wave” speed vector. The solution is the same Gaussian shape translated across the domain at speed and direction \vec{c} .

The Gaussian density concentration is translated the same total distance for each mesh size. Additionally the time step is chosen to be small enough such that the temporal accuracy has a negligible effect when compared to the spatial accuracy. In the cases presented here a time step $\Delta t = 10^{-5}$ with 1000 steps and $c = 1$ is chosen such that the Gaussian is translated a distance $x = 0.01$ in nominal domain size of 1.0 by 1.0. The choice of the direction \vec{c} depended on the mesh type. For all the test meshes the propagation is chosen to be in the x -direction, except for the sheared mesh, which is chosen in the y -direction. These propagation directions are chosen such that the deformation is “experienced” by the Gaussian. For the sheared mesh case the y -direction is chosen based on how the shear deformation is applied. In the stretched mesh case either direction is acceptable.

5.3. Poisson's equation

A 2D Poisson's equation is solved:

$$\nabla^2 \phi = S, \quad (5.2)$$

where ϕ is a scalar field, and S is a source forcing function. In this case S is chosen such that the solution is a Gaussian:

$$S = -4A \left[\left((x - x_0)^2 + (y - y_0)^2 \right) / r_c^4 \right] e^{-((x-x_0)^2 + (y-y_0)^2) / r_c^2}, \quad (5.3)$$

where A is the amplitude of the Gaussian, x_0 and y_0 are the center coordinates, and r_c characterizes the width of the Gaussian. The source is initialized in the center (centroid) of the mesh, such that the resulting solution is a Gaussian also at the centroid.

5.4. Linearized MHD equations

A linearized MHD system of equations is solved:

$$\begin{aligned} \rho \frac{\partial \mathbf{v}}{\partial t} &= \mathbf{j} \times \mathbf{B} - \nabla p, & \mathbf{j} &= \nabla \times \mathbf{b}, \\ \frac{\partial \mathbf{b}}{\partial t} &= \nabla \times (\mathbf{v} \times \mathbf{B}), & \nabla \cdot \mathbf{b} &= 0, \\ \frac{\partial p}{\partial t} + \gamma P \nabla \cdot \mathbf{v} &= 0, \end{aligned} \quad (5.4)$$

where $\mathbf{B} \equiv B\hat{n}$, and \mathbf{b} is the magnetic field perturbation. The form of a linear perturbation is: $\mathbf{v}(\mathbf{x}, t) = \mathbf{v}_0 \exp[i(\mathbf{k} \cdot \mathbf{x} - \omega t)]$. The eigensystem of these equations is solved and used to initialize the simulation for a particular MHD wave. Using this

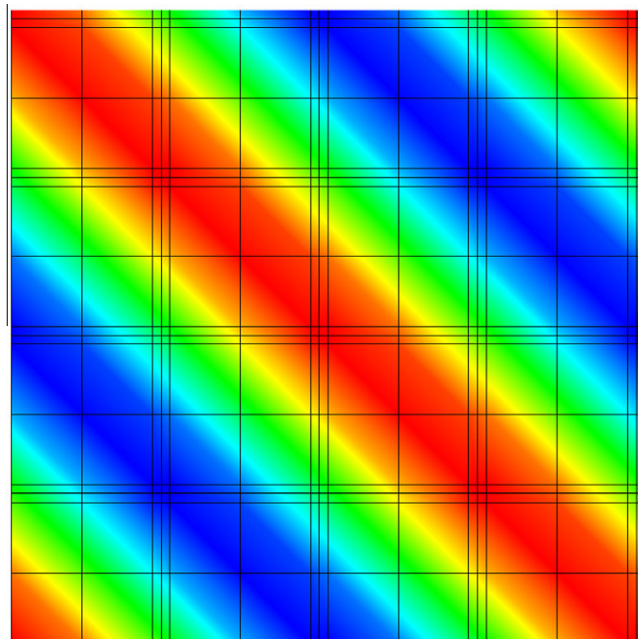
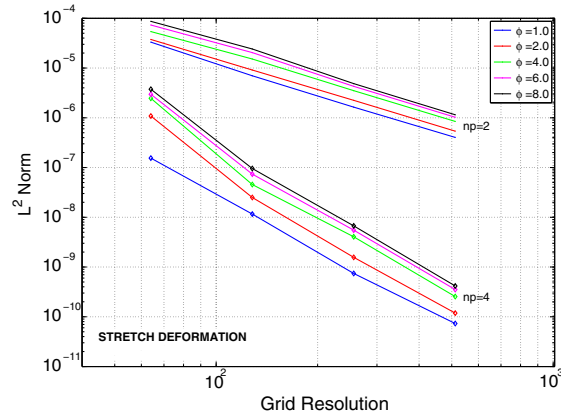
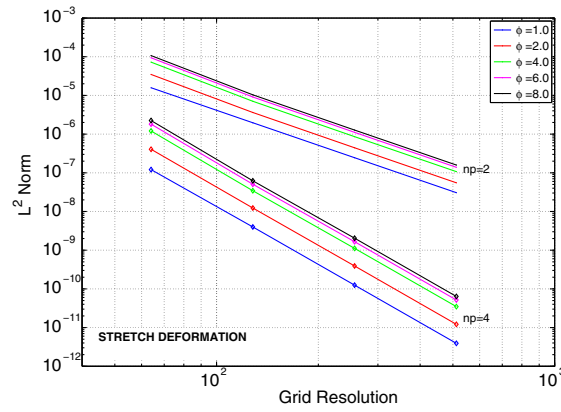


Fig. 9. Example linearized MHD initialization in a doubly periodic domain with a stretch deformation.

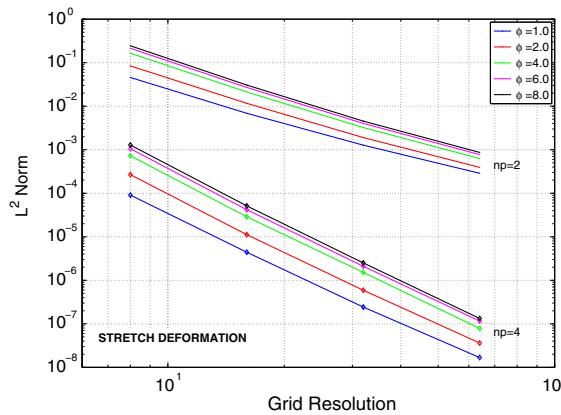
technique a pure wave is initialized with a known frequency and amplitude. In this study the slow magnetosonic wave is initialized and propagated in a doubly periodic domain at a 45° angle with respect to a uniform magnetic field aligned in the \hat{x} -direction. The solution is known because it is simply the translation of this wave in the domain propagated in the \hat{k} -direction. Fig. 9 shows an example wave in a mesh with a stretch deformation.



(a) Advection Equation



(b) Poisson's Equation



(c) Linearized MHD Equations

Fig. 10. Advection equation (a), Poisson's equation (b), and Linearized MHD (c) L^2 norm versus grid resolution for varying degrees of stretch and for both $np = 2$ and $np = 4$.

6. Results

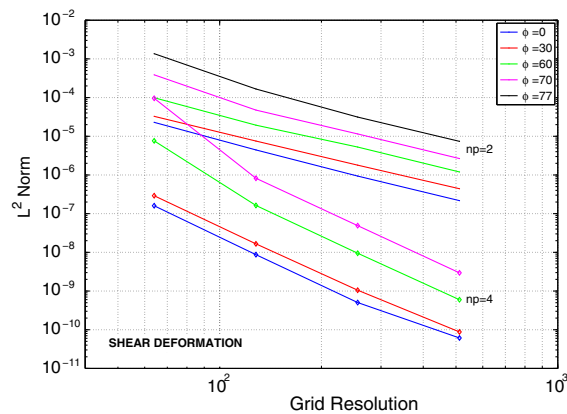
6.1. Order accuracy with varying deformations

The three test problems are solved for each of the test meshes (Figs. 10–14) with varying degree of deformation, varying spatial resolution, as well as for different polynomial orders of the basis function np of 2 (quadratic) and 4 (quartic). Boundary effects are minimized by using periodic domains and limiting the solution to near the domain centroid (advection and Poisson's equations). Tiling the domain with uniformly distorted meshes ensures the distortion affects all points of the solution and eliminates any boundary effects.

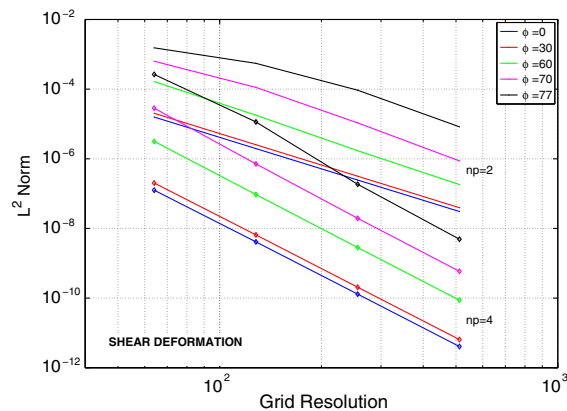
A normalized time-step $\Delta t = 10^{-5}$, which is much smaller than the characteristic time-scales of the test problems, is used to prevent the temporal order of the solver (second order Crank–Nicholson) impacting the solution accuracy. Additionally, only smooth solutions are chosen, since C^0 finite elements inherently produce numerical oscillations when attempting to resolve non-smooth solutions.

The resulting solutions are compared to the analytical solution and an L^2 error norm is calculated. The error norm is computed for varying spatial resolution, order of the basis functions, and degree of grid deformation. Figs. 10–14 show the L^2 error norm versus spatial resolution on a logarithmic scale for the different deformation types solving the advection equation, Poisson's equation, and the linearized MHD equations.

Looking at the L^2 error norm for each of the cases allows a baseline (no deformation) result to be compared to the formal accuracy of the method, as well as to determine how the different grid deformations deviate from the baseline calculation. For each case it is observed that increasing the level of mesh deformation does not reduce the order of the spatial accuracy of the method, but it does increase the magnitude of the error. Notice the lines plotted on a logarithmic scale in Figs. 10–14 are generally parallel with the slope given by the polynomial order np , demonstrating the order does not change. The distortions do however scale the solution error L^2 error norm by some factor d :

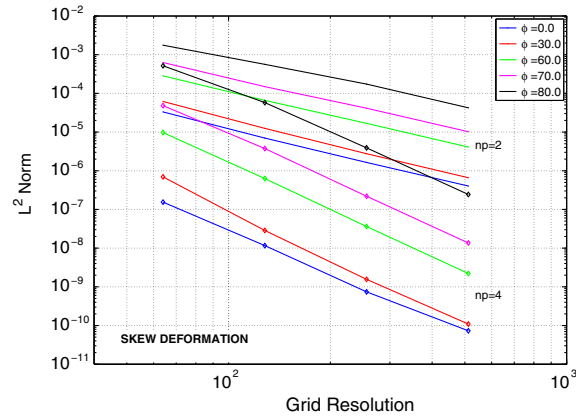


(a) Advection Equation

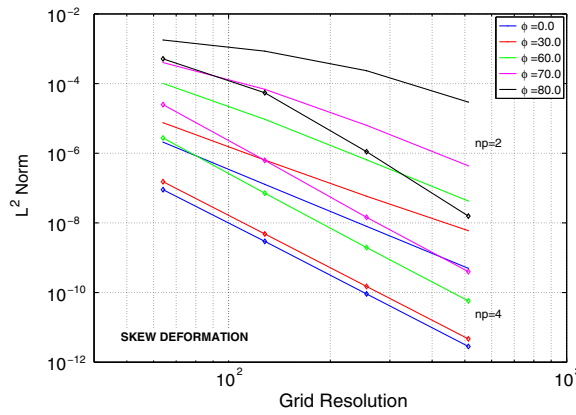


(b) Poisson's Equation

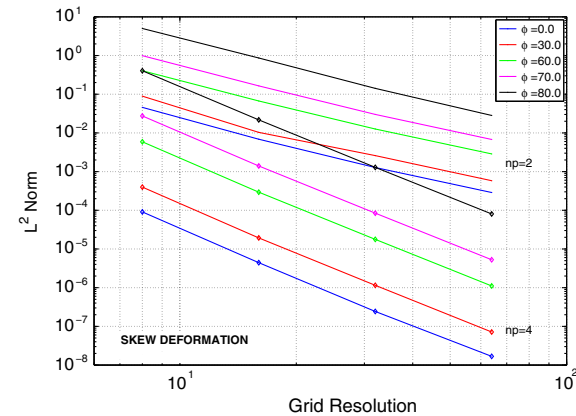
Fig. 11. Advection equation (a) and Poisson's equation (b) L^2 norm versus grid resolution for varying shear angles and for both $np = 2$ and $np = 4$.



(a) Advection Equation



(b) Poisson's Equation

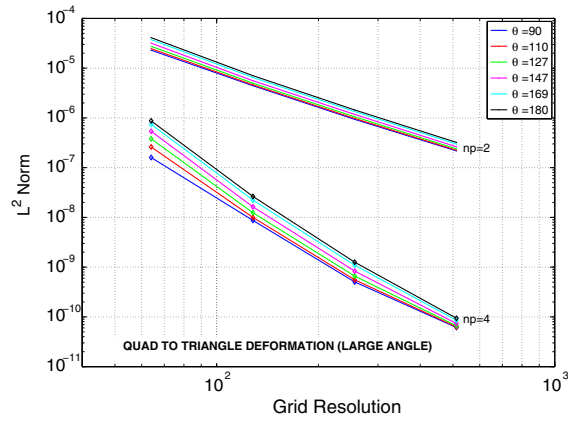


(c) Linearized MHD Equations

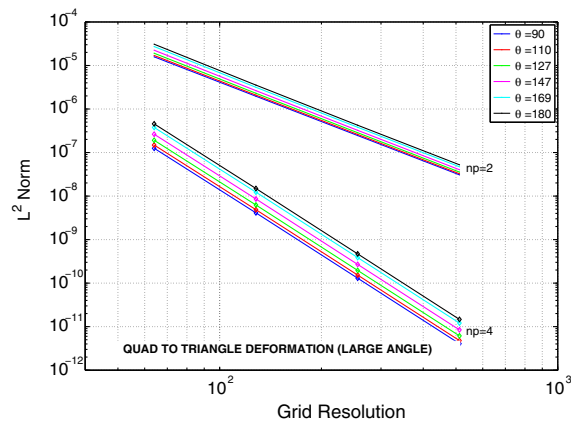
Fig. 12. Advection equation (a), Poisson's equation (b), and Linearized MHD (c) L^2 norm versus grid resolution for varying skew angles and for both $np = 2$ and $np = 4$.

$$\|E\|_2 = d\|E_0\|_2 = \mathcal{O}(\Delta x^n), \tag{6.1}$$

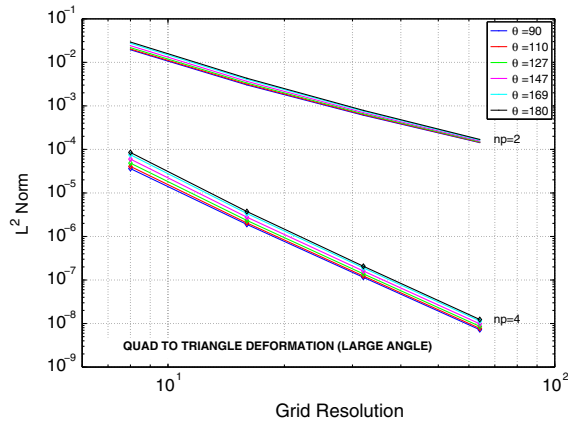
where $\|E_0\|_2$ is the L^2 error norm of the undistorted mesh. This result is consistent with theory and demonstrates that the convergence rates for different degrees of deformation preserve the order of spatial discretization, although the total error magnitude increases with higher degree of mesh deformation.



(a) Advection Equation



(b) Poisson's Equation

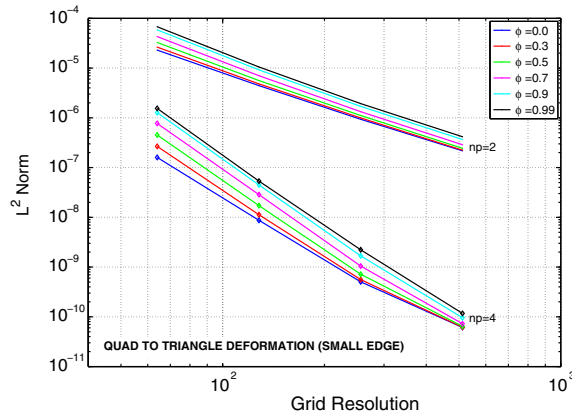


(c) Linearized MHD Equations

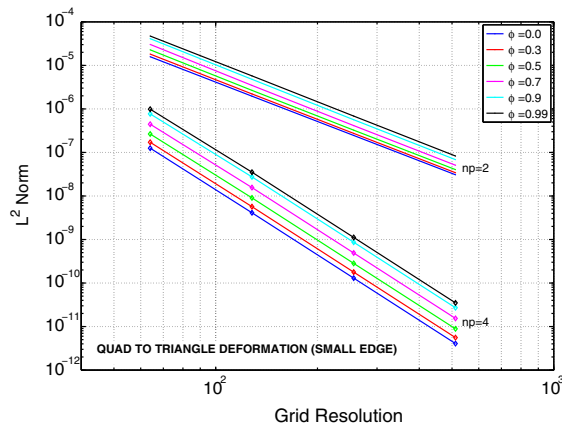
Fig. 13. Advection equation (a), Poisson's equation (b), and Linearized MHD (c) L^2 norm versus grid resolution for varying deformation degrees (large angle from 90° to 180°) and for both $np = 2$ and $np = 4$.

6.2. Solution error and mesh quality metrics

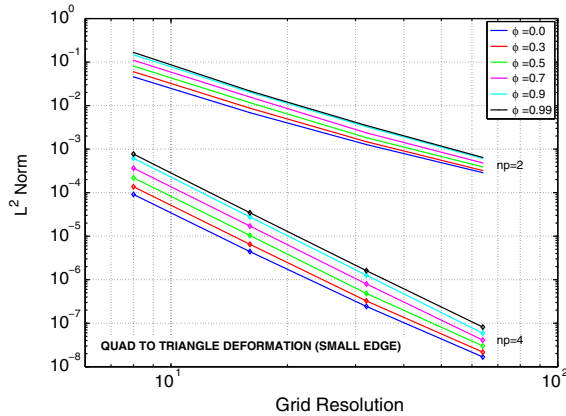
The mesh quality metrics depend solely on the mesh geometry and know nothing about the equations being solved or the solution. Here a correlation between the metrics and the solution error is investigated. The desired outcome is the determination of a metric that can be used as the indicator of a potential solution error, or at least to identify areas of the mesh that need improvement.



(a) Advection Equation



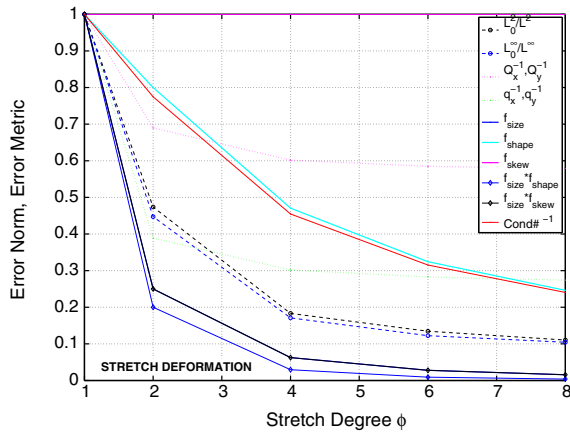
(b) Poisson's Equation



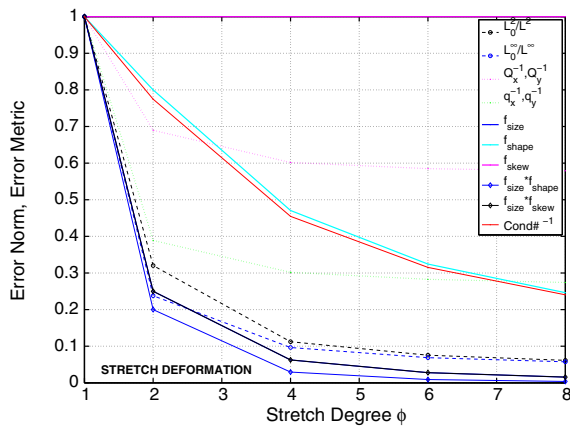
(c) Linearized MHD Equations

Fig. 14. Advection equation (a), Poisson's equation (b), and Linearized MHD (c) L^2 norm versus grid resolution for varying deformation degrees (small edge from length 1 to length 0) and for both $np = 2$ and $np = 4$.

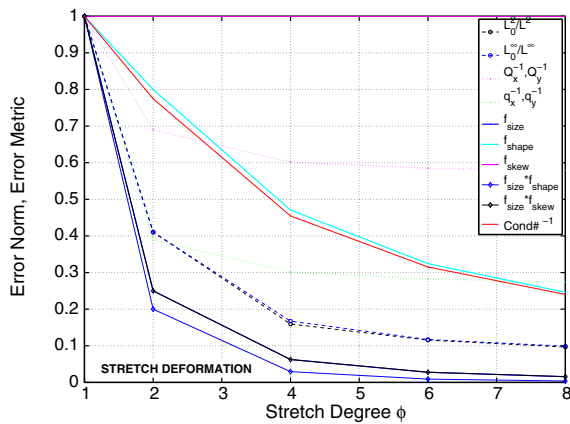
The error metrics defined in Sections 4.1 and 4.2, as well as stiffness matrix condition number defined in Section 4.3 are plotted along with the solution error norms calculated for test problems in Figs. 15–19. The metrics as well as the inverse of the L^2 norm are normalized such that 1 is the undeformed case, and 0 is the degenerate case. Knupp's metrics are defined on the scale from 0 to 1, and thus do not require normalization. Taking advantage of this characteristic, the products of Knupp metrics is also plotted. Figs. 15(a),(b), 16(a),(b), 17(a),(b), 18(a),(b), and 19(a),(b) are for the advection equation and Poisson's equation on the stretched, sheared, skewed, large angle, and small edge meshes respectively, and Figs. 15(c), 17(c),



(a) Advection Equation



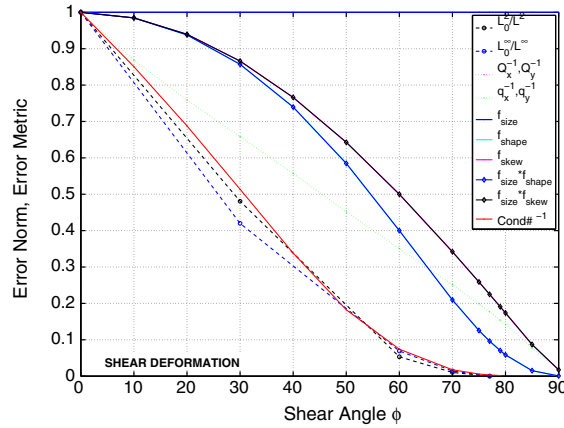
(b) Poisson's Equation



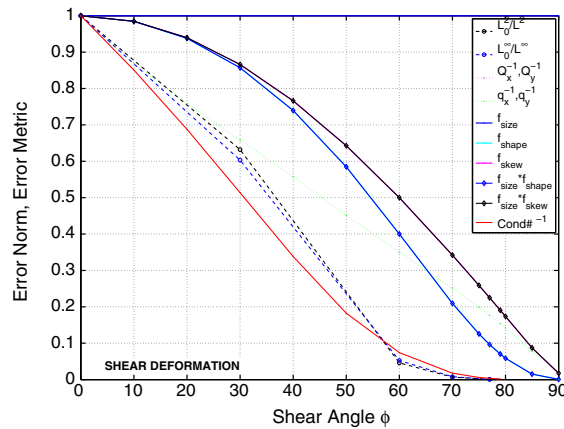
(c) Linearized MHD Equations

Fig. 15. Advection equation (a), Poisson's equation (b), and Linearized MHD (c) inverse error norms and mesh quality metrics (Section 4) for a stretch deformation. Error norms and metrics are normalized (if necessary) to range from 1 to 0, where 1 is an undeformed element, and 0 is degenerate element. Both the inverse L^2 norm and the inverse L^∞ norm are plotted. Q_x^{-1} and q_x^{-1} are in the 1st and 2nd order inverse Kallinderis/Kontzialis metrics, f_{size} , f_{shape} , and f_{skew} are the Knupp metrics. Products of the Knupp metrics are also included. $Cond^{-1}$ is the inverse stiffness matrix condition number.

18(c) and 19(c) are for the linearized MHD equations. Each of these cases has a fixed resolution of 256×256 with $np = 4$. For each of the mesh types and for the three test problems it can be seen that the error norms follow the same trend as some of the error metrics.



(a) Advection Equation



(b) Poisson's Equation

Fig. 16. Advection equation (a) and Poisson's equation (b) inverse error norms and error metrics for a shear deformation. Error norms and mesh quality metrics (Section 4) are normalized (if necessary) to range from 1 to 0, where 1 is an undeformed element, and 0 is degenerate element. Both the inverse L^2 norm and the inverse L^∞ norm are plotted. Q_x^{-1} and q_x^{-1} are in the 1st and 2nd order inverse Kallinderis/Kontzialis metrics, f_{size} , f_{shape} , and f_{skew} are the Knupp metrics. Products of the Knupp metrics are also included. $Cond^{-1}$ is the inverse stiffness matrix condition number.

In order to quantify the correlation between the solution error norms and the mesh deformation metrics, a χ^2 goodness of fit test statistic is calculated for the error norms compared to the expected mesh metric value. In this case the solution norm is the observed quantity and the mesh deformation metric is the expected quantity. The goodness of fit test statistic is defined as:

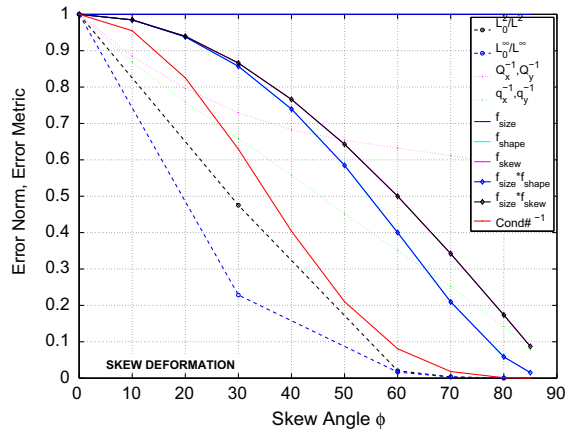
$$\chi^2 = \sum_{i=1}^n \frac{(O_i - E_i)^2}{E_i} \tag{6.2}$$

where O_i are the observed solution error norms, and E_i are the expected mesh deformation metric values. Table 1 has the test statistic values for each of the mesh metrics and different mesh deformation types for each of the test problems.

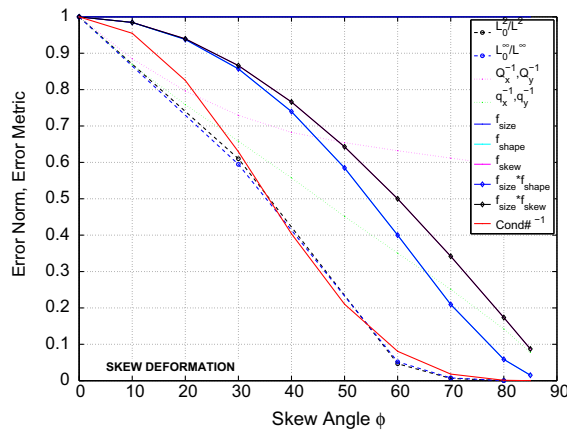
The closer the test values are to 0 the higher the probability that the expected value will be met. It is observed that for all but the skew deformation type the solution error norm has the highest probability of following the Knupp metric for all test problems. However, in the skew case the stiffness matrix condition number has the lowest χ^2 test statistic. In order to provide some context, when comparing the metrics to a problem whose error does not increase with increasing deformation (e.g. metric is constant at 1.0) the χ^2 value is approximately 0.5. Thus, relative to $\chi^2 = 0.5$, it is reasonable to assume that the metrics with $\chi^2 < 0.25$ provide statistically significant correlation to solution error.

7. Conclusion

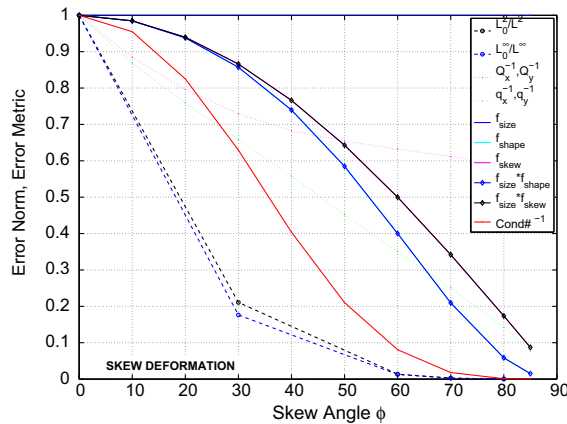
The results of this study show that for the typical types of elemental mesh distortions and representative differential operators (namely, those in the advection, Poisson's, and linearized MHD equations) the spatial order of the spectral element



(a) Advection Equation



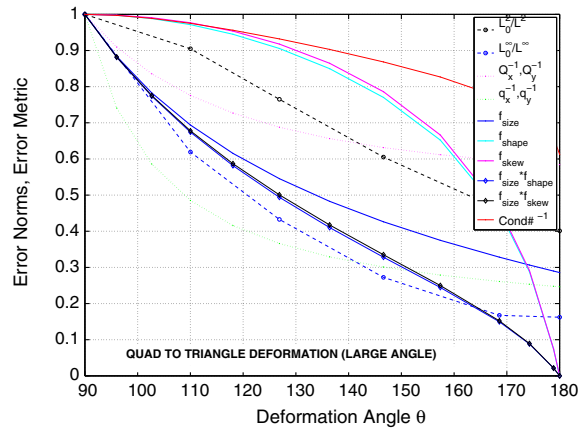
(b) Poisson's Equation



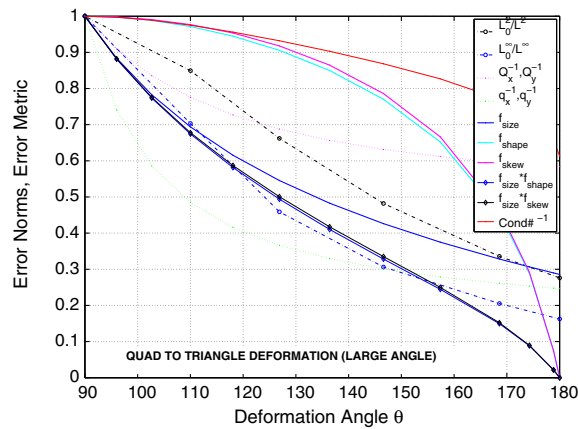
(c) Linearized MHD Equations

Fig. 17. Advection equation (a), Poisson's equation (b), and Linearized MHD (c) inverse error norms and mesh quality metrics (Section 4) for a skew deformation. Error norms and metrics are normalized (if necessary) to range from 1 to 0, where 1 is an undeformed element, and 0 is degenerate element. Both the inverse L^2 norm and the inverse L^∞ norm are plotted. Q_x^{-1} and q_y^{-1} are in the 1st and 2nd order inverse Kallinderis/Kontzialis metrics, f_{size} , f_{shape} , and f_{skew} are the Knupp metrics. Products of the Knupp metrics are also included. $Cond^{-1}$ is the inverse stiffness matrix condition number.

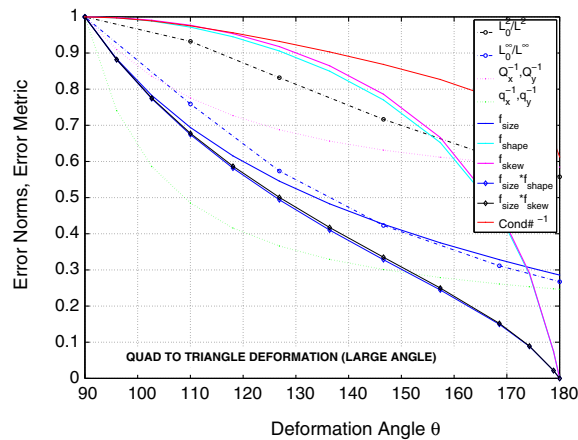
method is preserved with varying degrees of mesh distortion. However, the error is also shown to be a function of overall resolution. By plotting the metrics along with solution error norms, it is observed that the error trend is similar to that of the mesh metrics. This gives a good indication of how the metrics can predict solution error. Knowing that the spatial convergence rates are preserved, an appropriate mesh resolution and spectral element polynomial order can also be chosen for



(a) Advection Equation



(b) Poisson's Equation

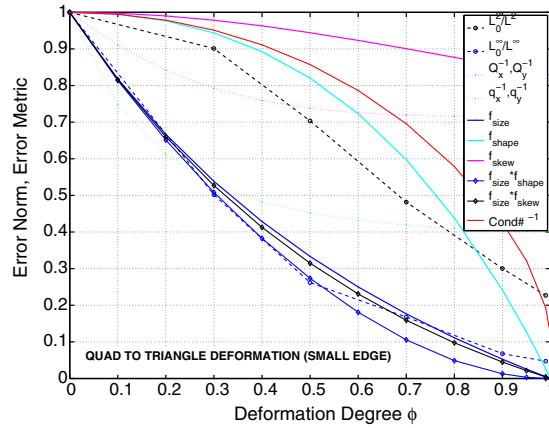


(c) Linearized MHD Equations

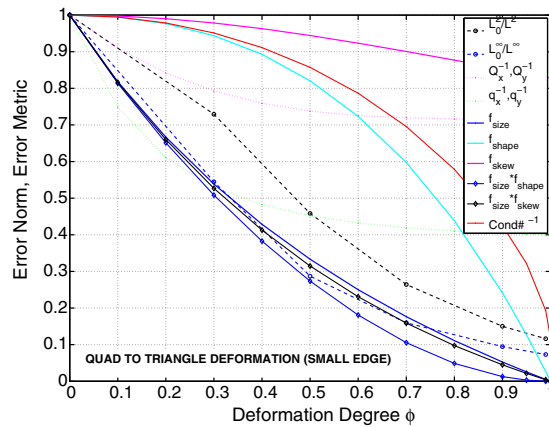
Fig. 18. Advection equation (a), Poisson's equation (b), and Linearized MHD (c) inverse error norms and mesh quality metrics (Section 4) for a large angle deformation. Error norms and metrics are normalized (if necessary) to range from 1 to 0, where 1 is an undeformed element, and 0 is degenerate element. Both the inverse L^2 norm and the inverse L^∞ norm are plotted. Q_x^{-1} and q_x^{-1} are in the 1st and 2nd order inverse Kallinderis/Kontzialis metrics, f_{size} , f_{shape} , and f_{skew} are the Knupp metrics. Products of the Knupp metrics are also included. $Cond\#^{-1}$ is the inverse stiffness matrix condition number.

target solution accuracy. This, in turn, suggests that locally increasing the resolution in regions of high grid distortion can improve the overall accuracy of the solution.

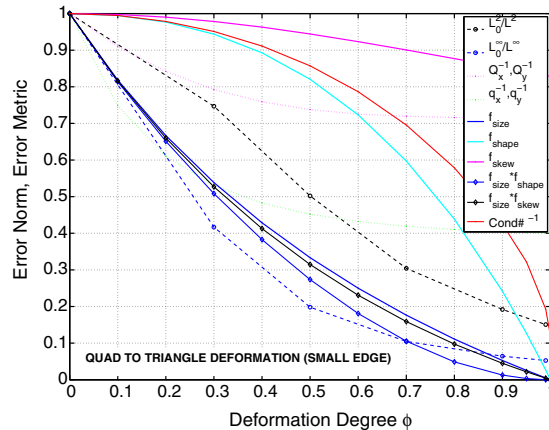
The variability of different equation sets and solutions increases the complexity of evaluating the mesh distortion effects, and one should remain cautious about how the mesh might influence their particular problem. Nevertheless, it has been



(a) Advection Equation



(b) Poisson's Equation



(c) Linearized MHD Equations

Fig. 19. Advection equation (a), Poisson's equation (b), and Linearized MHD (c) inverse error norms and mesh quality metrics (Section 4) for a small edge deformation. Error norms and metrics are normalized (if necessary) to range from 1 to 0, where 1 is an undeformed element, and 0 is degenerate element. Both the inverse L^2 norm and the inverse L^∞ norm are plotted. Q_x^{-1} and q_y^{-1} are in the 1st and 2nd order inverse Kallinderis/Kontzialis metrics, f_{size} , f_{shape} , and f_{skew} are the Knupp metrics. Products of the Knupp metrics are also included. $Cond^{-1}$ is the inverse stiffness matrix condition number.

shown that some *a priori* metrics can provide a good estimate to potential error in the solution and are a useful tool in mesh creation and analysis. One must note that the analysis presented here makes a careful attempt to minimize boundary effects by keeping the solution near zero at boundaries and/or use of periodic boundary conditions. The present analysis also uses a regular tiling of the mesh which amounts to approximately homogenous sized elements. Additionally only smooth isotropic

Table 1

χ^2 goodness of fit test values for Poisson's equation, the advection equation, and linearized MHD equation's L^∞ and L^2 error norms compared to expected mesh metrics values, where q_x and Q_x are the Kallinderis/Kontzialis 2nd and 1st order metrics respectively, Knupp is the $f = f_{size} \times f_{skew}$ metric, and condition number is the stiffness matrix condition number.

		Stretch	Skew	Large angle	Small edge
<i>Poisson's equation</i>					
q_x	L^∞	3.390×10^{-2}	3.150×10^{-2}	1.810×10^{-2}	6.160×10^{-2}
	L^2	2.661×10^{-2}	3.161×10^{-2}	6.795×10^{-2}	4.505×10^{-2}
Q_x	L^∞	2.417×10^{-1}	2.472×10^{-1}	9.530×10^{-2}	2.674×10^{-1}
	L^2	2.168×10^{-1}	2.480×10^{-1}	3.618×10^{-2}	1.868×10^{-1}
Knupp	L^∞	4.453×10^{-4}	5.990×10^{-2}	9.916×10^{-4}	8.319×10^{-4}
	L^2	1.395×10^{-3}	9.467×10^{-2}	2.458×10^{-2}	2.165×10^{-2}
Condition number	L^∞	1.572×10^{-1}	5.875×10^{-4}	2.038×10^{-1}	2.050×10^{-1}
	L^2	1.217×10^{-1}	2.326×10^{-4}	9.430×10^{-2}	1.035×10^{-1}
<i>Advection equation</i>					
q_x	L^∞	1.550×10^{-2}	1.092×10^{-1}	9.200×10^{-3}	7.000×10^{-2}
	L^2	1.472×10^{-2}	4.790×10^{-2}	1.182×10^{-1}	6.018×10^{-2}
Q_x	L^∞	1.621×10^{-1}	3.224×10^{-1}	1.132×10^{-1}	2.884×10^{-1}
	L^2	1.524×10^{-1}	2.701×10^{-1}	1.518×10^{-2}	9.253×10^{-2}
Knupp	L^∞	1.250×10^{-2}	2.095×10^{-1}	2.700×10^{-3}	3.774×10^{-4}
	L^2	1.300×10^{-2}	1.359×10^{-1}	5.899×10^{-2}	1.005×10^{-1}
Condition number	L^∞	6.910×10^{-2}	7.230×10^{-2}	2.354×10^{-1}	2.240×10^{-1}
	L^2	6.010×10^{-2}	1.087×10^{-2}	4.242×10^{-2}	1.837×10^{-2}
<i>MHD equation</i>					
q_x	L^∞	1.560×10^{-2}	1.289×10^{-1}	3.610×10^{-2}	8.690×10^{-2}
	L^2	1.632×10^{-2}	1.159×10^{-1}	1.784×10^{-1}	3.762×10^{-2}
Q_x	L^∞	1.706×10^{-1}	3.388×10^{-1}	4.530×10^{-2}	3.270×10^{-1}
	L^2	1.729×10^{-1}	3.283×10^{-1}	1.210×10^{-2}	1.587×10^{-1}
Knupp	L^∞	9.200×10^{-3}	2.402×10^{-1}	8.100×10^{-3}	4.300×10^{-3}
	L^2	6.903×10^{-3}	2.490×10^{-1}	9.704×10^{-2}	2.918×10^{-2}
Condition number	L^∞	8.030×10^{-2}	9.230×10^{-2}	1.263×10^{-1}	2.831×10^{-1}
	L^2	8.131×10^{-2}	7.881×10^{-2}	1.182×10^{-2}	8.315×10^{-2}

solutions are considered. When one solves more realistic problems that have boundary effects, more complex boundary conditions, non-smooth, and anisotropic solutions on more realistic heterogeneous meshes – the error predictions are naturally more difficult to quantify. However, even under such circumstances, the analysis presented here can lead to a reliable predictor of the location and magnitude of the highest solution error associated with the greatest distortion of the computational mesh.

In this study, the spectral stiffness matrix condition number, and the product of the Knupp metrics provided the most consistent metrics when comparing to the test problem solution error. Both of these metrics are formulated for finite elements (linear finite elements in the Knupp case), while the Kallinderis metric is formulated for a finite volume type approach. The stiffness matrix condition number is a global measure and is the most computationally intensive metric to calculate. Since the Knupp and Kallinderis metrics are local (element wise) measures, they are quick to calculate, which makes them attractive when dealing with large meshes.

All of the analysis presented in this manuscript is done in 2D, but it is expected that these results extend to 3D. Similar corollary to the 2D meshes can be imagined in 3D (i.e. stretch, shear, skew, etc.), and this is the subject of a future study.

Acknowledgments

This research was supported by the US Department of Energy and the Office of Naval Research. Special thanks to Alan Glasser, Ulrich Hetmaniuk, and Eric Meier for their help and advice with this research.

References

- [1] P.M. Knupp, Algebraic mesh quality measures, *SIAM J. Comput. Phys.* 23 (2001) 193–218.
- [2] P.M. Knupp, Remarks on mesh quality, in: 45th AIAA Aerospace Science Meeting and Exhibit, Reno, NV, 7–10 January, 2007.
- [3] P.M. Knupp, Algebraic mesh quality metrics for unstructured initial meshes, *Finite Elem. Anal. Des.* 39 (2003) 217–241.
- [4] P.M. Knupp, Label-invariant mesh quality metrics, in: Proceedings of the 18th International Meshing Roundtable, Part 3, 2009, pp. 139–155.
- [5] M. Berzins, Mesh quality: a function of geometry, error estimates or both?, *Eng Comput.* 15 (1999) 236–247.
- [6] B. Cockburn, P. Gresho, *A priori* error estimates for numerical methods for scalar conservation laws. Part II: flux-splitting monotone schemes on irregular Cartesian grids, *Math. Comput.* 66 (1997) 547–572.

- [7] Y. Kallinderis, C. Kontzialis, *A priori* mesh quality estimation via direct relation between truncation error and mesh distortion, *J. Comput. Phys.* 228 (2009) 881–902.
- [8] K.K. Okamoto, G.H. Klopfer, J.J. Chattot, *Assessing grid quality of structured meshes by truncation error analysis*, Fifteenth International Conference on Numerical Methods in Fluid Dynamics, vol. 490, Springer, Berlin, Heidelberg, 1997.
- [9] I. Babuška, A.K. Aziz, On the angle condition in the finite element method, *SIAM J. Numer. Anal.* 13 (1976) 214–226.
- [10] L.A. Freitag, P.M. Knupp, Tetrahedral mesh improvement via optimization of the element condition number, *Int. J. Numer. Methods Eng.* 53 (2002) 1377–1391.
- [11] I. Tsukerman, A general accuracy criterion for finite element approximation, *IEEE Trans. Magn.* 34 (1998) 2425–2428.
- [12] F.-X. Zgainski, Y. Marechal, J.-L. Coulomb, An *a priori* indicator of finite element quality based on the condition number of the stiffness matrix, *IEEE Trans. Magn.* 33 (1997) 1748–1751.
- [13] M.L. Bittencourt, T.G. Vazquez, A nodal spectral stiffness matrix for the finite-element method, *IMA J. Appl. Math.* 73 (2008) 837–849.
- [14] A.H. Glasser, X.Z. Tang, The SEL macroscopic modeling code, *Comput. Phys. Commun.* 164 (2004) 237–243.
- [15] V.S. Lukin, Ph.D. Dissertation, Princeton University, 2007.
- [16] V.S. Lukin, A.H. Glasser, W. Lowrie, E.T. Meier, Overview of HiFi – implicit spectral element code framework for general multi-fluid applications. *J. Comput. Phys.*, manuscript in preparation.
- [17] V. Hernandez, J.E. Roman, V. Vidal, SLEPc: a scalable and flexible toolkit for the solution of eigenvalue problems, *ACM Trans. Math. Softw.* 31 (3) (2005) 351–362. <<http://www.grycap.upv.es/slep/>>.